Analytical electron microscopy study on gallium nitride systems doped with manganese and iron

2015 Semicond. Sci. Technol. 30 035002

(http://iopscience.iop.org/0268-1242/30/3/035002)

OPEN ACCESS
IOP Publishing
Semiconductor Science and Technology
Semicond. Sci. Technol. **30** (2015) 035002 (9pp)
doi:10.1088/0268-1242/30/3/035002

Analytical electron microscopy study on gallium nitride systems doped with manganese and iron

Arno Meingast[1,2], Andrea Navarro Quezada[3], Thibaut Devillers[3], András Kovács[4], Mihela Albu[1,2], Stefanie Fladischer[1,2], Alberta Bonanni[3] and Gerald Kothleitner[1,2]

[1] Institute for Electron Microscopy and Nanoanalysis, Graz University of Technology, Steyrergasse 17, 8010 Graz, Austria,
[2] Graz Centre for Electron Microscopy, Steyrergasse 17, 8010 Graz, Austria
[3] Institut für Halbleiter- und Festkörperphysik, Johannes Kepler University, Altenbergerstrasse 69, 4040 Linz, Austria
[4] Ernst Ruska-Centrum für Mikroskopie und Spektroskopie mit Elektronen, Forschungszentrum Jülich GmbH, 52425 Jülich, Germany

E-mail: arno.meingast@felmi-zfe.at

Received 30 July 2014, revised 26 November 2014
Accepted for publication 9 December 2014
Published 8 January 2015

Abstract

Modulated structures of gallium nitride (GaN) doped with transition metal ions (here Fe, Mn) are investigated by analytical (scanning) transmission electron microscopy to gain insight into the structural arrangement and chemical composition of the material, known to be critically correlated to the magnetic response and hence the functionality of these technologically relevant systems. Three classes of samples are considered: (i) homogeneous (dilute) (Ga, Mn)N; (ii) δ-Mn-doped (Ga, δ-Mn)N and phase separated (Ga, Fe)N, containing Fe-rich nanocrystals. The combination of various microscopic techniques employed, allows for a quantitative determination of the distribution of the magnetic ions in the samples, providing essential information on the structural and chemical asset of these systems.

Keywords: electron microscopy, gallium nitride, manganese, iron

(Some figures may appear in colour only in the online journal)

1. Introduction

Gallium nitride (GaN) based material systems are currently playing a key technological role, particularly in the field of optoelectronics and lighting for the future. It is expected that the addition of magnetic capabilities through doping with transition metals or rare earths, will extend the functionality of these materials systems to applications in spintronics, quantum information and magneto-optics [1–4]. A number of studies carried out over recent years, have highlighted how the distribution of magnetic dopants in the semiconducting matrix substantially affects the structural, magnetic, electrical and optical properties of the resulting material. In particular, the recent advancements in the fabrication and characterization of magnetically doped nitrides, have made clear that depending on the growth conditions and eventually on the post-growth treatment, the introduction of magnetic ions can essentially result in: (i) a dilute (homogeneous) system [5]; (ii) a chemically inhomogeneous system (chemical phase separation) [6]; (iii) a crystallographically inhomogeneous system (crystallographic phase separation, secondary phases, embedded nanocrystals) [7]; (iv) a system containing functional magnetic complexes [8].

With these premises, the control over the formation, structure, arrangement and effect of inhomogeneity on the

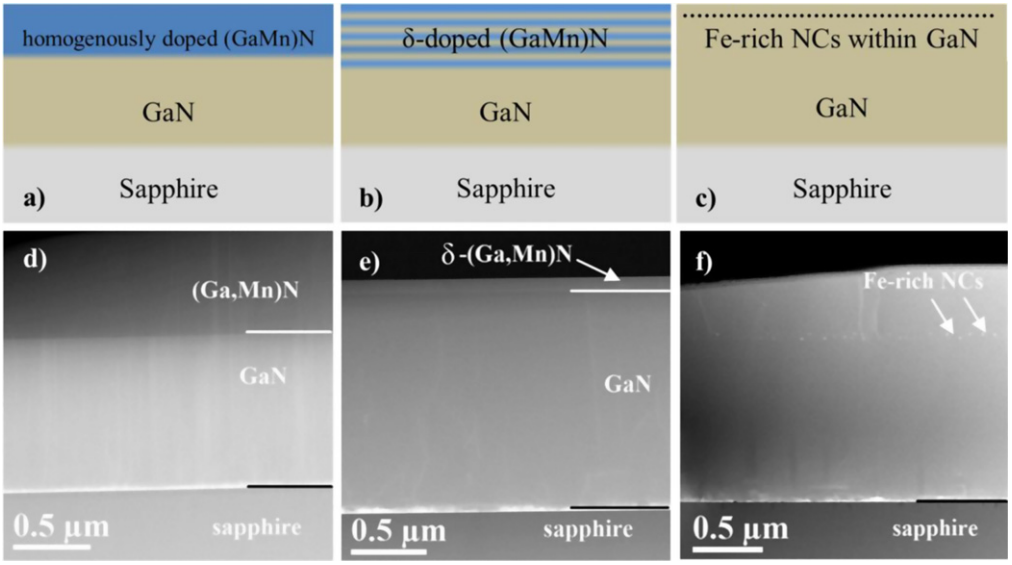

Figure 1. Schematic cross-sections not to scale of: (a) homogenously Mn doped GaN; (b) Mn δ-doped GaN; (c) Fe-rich nanocrystals; (d)–(e) corresponding STEM HAADF images in GaN [11–20] orientation depicting the various layers and precipitates.

chemical and physical behavior of the host material is essential for the design and functionality of the next generation of devices.

Recently, it has been demonstrated that superexchange interactions account for ferromagnetism in (Ga, Mn)N in the absence of free carriers [5, 9]. In order to reliably exploit this material system in functional devices such as e.g. a new generation of spin filters, a control of the effective Mn incorporation in GaN and of the interfaces of (Ga, Mn)N in heterostructures is necessary [10].

Particularly in the case of embedded magnetic nanocrystals, it is essential to establish the correlation between the growth parameters and the local chemical composition and size of the nanostructures, considering that these figures have been shown to determine the magnetic properties of the whole system. For instance, in the case of Fe-rich nanocrystals embedded in GaN, it is found that by modifying the composition of the nanostructures, it is possible to tune the system from ferromagnetic to antiferromagnetic up to room temperature. Here the formation of magnetic Fe-rich nanocrystals paves the way to the realization of non-volatile flash-memories and tunable ferromagnetic/antiferromagnetic spintronic devices based on these hybrid systems [11].

In this work, electron microscopic techniques are applied to dilute (Ga, Mn)N systems, to two-dimensional (2D) layers of (Ga, Mn)N embedded in GaN, and to planar arrays of Fe-rich nanocrystals embedded in GaN.

2. Material and methods

All the samples considered are fabricated by metalorganic vapor phase epitaxy on *c*-sapphire, according to the procedures reported elsewhere and have been thoroughly characterized with respect to their magnetic and optical properties via both conventional and synchrotron radiation-based techniques [5–7]. The microscopic and chemically-sensitive investigations of the structures are the focus of this work.

For the dilute (Ga, Mn), 2D (Ga, Mn)N layers and planar array of Fe-rich nanocrystals, schematic cross sections and their scanning transmission electron microscope (STEM) image counterparts (oriented along the GaN [11–20] zone-axis) are shown in figure 1. In the homogenous Mn co-doping process, a layer thickness of 700 nm is realized with a nominal concentration of 1.55 at% of Mn atoms within GaN. The 2D (Ga, Mn)N layers, having a total thickness of 150 nm, are obtained through δ-doping, a process realized by periodically providing Mn flow during GaN growth. Hereby, the starting point has been a sample with an averaged concentration of nominal 1.30 at% of Mn atoms within GaN. Samples of (Ga, Fe)N above the solubility limit of Fe, with crystallographic and chemically phase separated regions present, are investigated in addition. The growth conditions are given in [8]. The nominal Fe concentrations are 0.25% and 0.5%, respectively, found by secondary ion mass spectrometry (SIMS) in each case.

All cross-section specimens have been fabricated by mechanical polishing utilizing a semi-automated 8″ Platen MultiPrep system from Allied High Tech. Ion-thinning has been performed by using a PIPS-system (Gatan Inc.) with Ar ions at 3, 4 kV voltage and 4° incident angle until perforation of the film. The final polishing step has then been performed on a Gentle Mill system (Technoorg Linda) at 500 eV with an incident angle of 14° for 30 min. This procedure has been repeated typically two to three times while observing the milling quality in the transmission electron microscope (TEM) until the specimen surface has exhibited a sufficient amorphous-free surface at the desired specimen position as visualized in figure 2, exemplified for the nanocrystal case.

The TEM and STEM investigations have been performed on different instruments depending on the equipment needed. Specimen orientations have been either along GaN [11–20] or

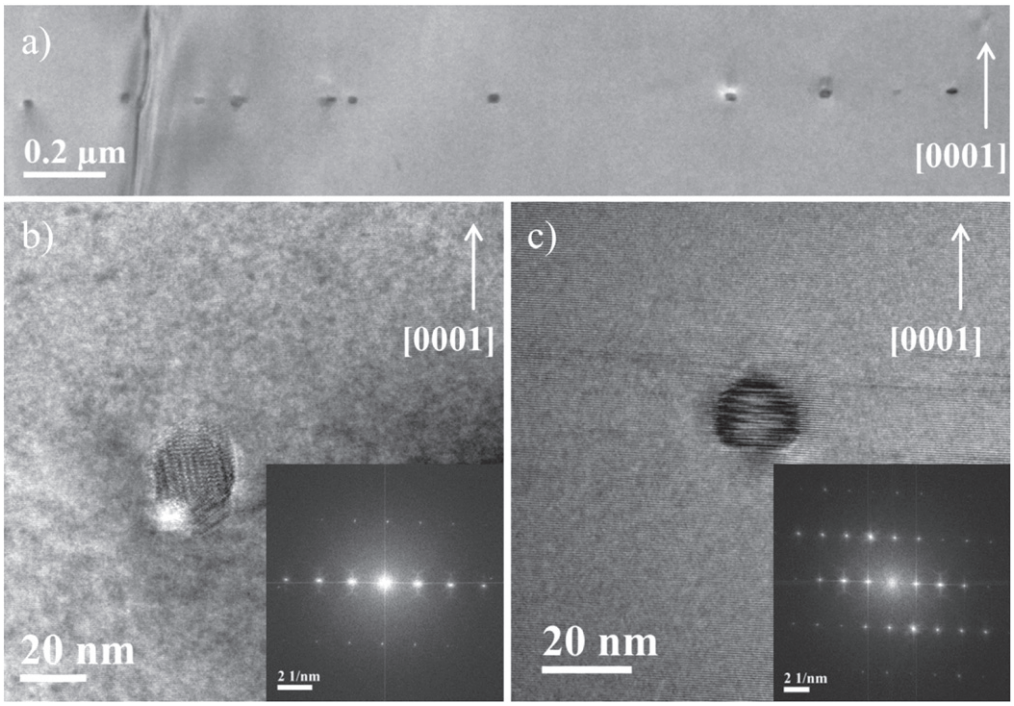

Figure 2. Bright field images of nanocrystals in GaN: (a) larger-scale image, depicting their density; (b) exhibiting considerable surface amorphization; inset: FFT with reduced information limit caused by amorphization; (c) sample area after low voltage milling.

close to this orientation, unless the sample has been tilted towards the energy dispersive x-ray spectroscopy (EDXS) detector, merely for maximum signal-collection. Conventional bright field TEM imaging investigations have been carried out on a Tecnai 200 kV FEG microscope from FEI, equipped with a Gatan GIF Tridiem electron energy loss spectroscopy (EELS) spectrometer [12] and an EDAX Phoenix Si(Li) x-ray detection system. This system has been used to record the energy filtered transmission electron microscopy (EFTEM) images as jump-ratio maps from the Mn L_{23} edge with a slit-width of 30 eV collected at 620 eV and 655 eV.

Furthermore, this system has been utilized for the quantitative analysis of the Fe-rich nanocrystals via EELS and EDXS reported later in this work. X-ray spectra have been subjected to a ζ-factor analysis, using the software-package written by Watanabe [13–15]. For the evaluation of concentrations, the peak intensities Kα signals of N, O, Ga and Fe have been extracted by removing the background through bilinear interpolation, left and right of the respective line. Data acquisition has been performed by scanning a region of interest (50×50 pixels) across the central part of the individual nanocrystals. Hereby, a dwell-time of 15 μs and a beam-current ranging from 150 pA to 250 pA have been used, accounting better for beam-induced modifications of the nanocrystal. Each nanocrystal has been measured only once to avoid erroneous measurements on possibly beam-modified material. In the case of visible heterogeneities in the crystal, individual, spatially resolved spectra have been recorded as spectrum images. The specimens investigated (with nominal Fe concentration of 0.25% and 0.5%) have been tilted 15° towards the x-ray detector to avoid strong channeling effects and maximize signal collection efficiency.

The collection angles for EELS are 15.9 mrad for a GIF Tridiem installed at the Tecnai 200 kV FEG instrument (utilized for nanocrystal quantification) and 40.4 mrad for a DualEELS capable GIF Quantum [16] installed at the TITAN instrument operated at 300 kV (utilized for both Mn-doped GaN quantifications), respectively. Processing of the EELS data has been carried out with DigitalMicrograph (Gatan Inc.) applying regular EELS quantification schemes, however, accounting also for multiple scattering by low-loss deconvolution. For the quantification of the EELS signals the K edges of N (as well as O) and the L_{23} edges of Ga and Fe have been collected. The background is modeled by a power-law function and Hartree–Slater cross-sections are employed for conversion into concentrations.

High resolution STEM investigations have been carried out on a 60–300 kV probe-C_s-corrected TITAN microscope. Corrector tunings have always been performed until an aberration-free zone of 19 mrad or better has been reached, giving a spatial resolution better than 1 Å.

Annular bright field (ABF) imaging has been utilized as an alternative technique in order to harness its sensitivity for structural changes and its possibility to image lighter N atoms [17–21]. To obtain ABF images it has been paramount to avoid carbon surface contamination and to reduce surface-amorphization with the procedures described earlier. In our setup the ABF image has been registered with an annular detector as described in [20], collecting the direct beam diffraction disk within an angular range between 10 and 20 mrad for a beam convergence of 20 mrad. A beam current of of ~80 pA and a pixel time of 20 μs have been used.

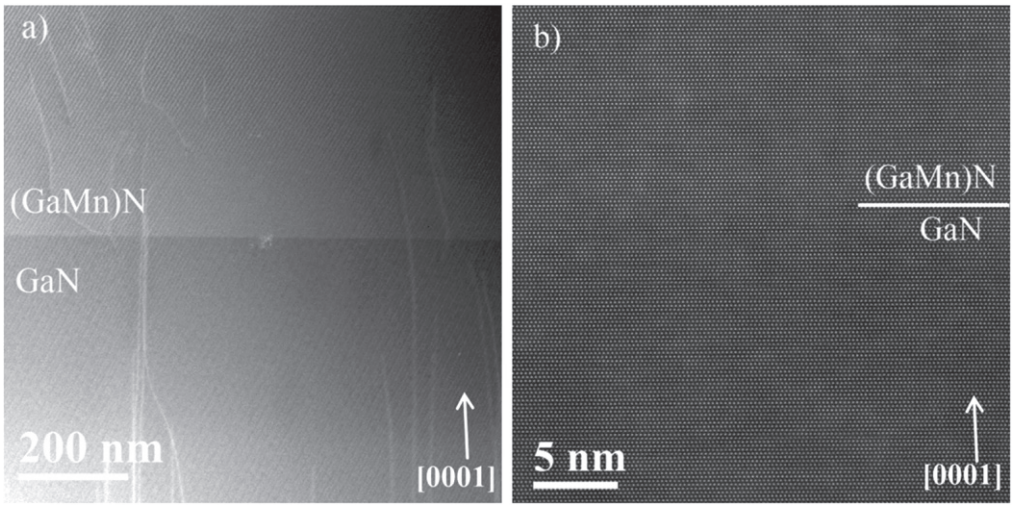

Figure 3. STEM HAADF images of: (a) GaN buffer and homogenously doped (GaMn)N layer showing an increased signal intensity for (GaMn)N compared to un-doped GaN; (b) no structural modifications at the interface are observed.

Corresponding HAADF images have been recorded with an angular range from 26 mrad to 95 mrad.

3. Results and discussion

3.1. Mn-doped GaN

To examine the structural homogeneity of the Mn-doped GaN samples, aberration-corrected HR-STEM investigations have been carried out. In figure 3(a) the interface between the GaN buffer and the doped part of the homogenously doped sample are shown. Dislocations originating at the interface substrate/GaN-buffer and propagating into the Mn-doped layer can be observed (in addition to a minor contamination spot in the field of view). All analytical measurements herein reported have been carried out at least 100 nm away from the dislocations. Structurally, at the interface GaN/(GaMn)N no significant lattice mismatch or crystallographic phase separation despite the rather high doping level (figure 3(b)) has been found. A geometrical phase analysis (GPA) [22] of the GaN/(GaMn)N interface has revealed strain at the interface being in the order of <1% (maps not shown). A faint brightness difference between the GaN/(GaMn)N interface can be identified due to changes in average Z, because of Mn having been mixed homogeneously into the otherwise nominally undoped GaN. An increase of ~2% in brightness can be identified when moving from GaN into (GaMn)N.

This intensity variation becomes more pronounced in figure 4, where the situation for the Mn δ-doped GaN is reported. A multi-layered structure is formed, leading δ-Mn regions. As evidenced in figure 4, the layers exhibit irregular periodicity and width.

High resolution HAADF and ABF images (figures 5(a) and (b)) have also been subject to a GPA analysis, and reveal no strain above 1%, indicating the coherent incorporation of Mn within the δ-doped region. A line-profile extracted from the HAADF signal (figure 5(c)) shows a sinusoidal-type

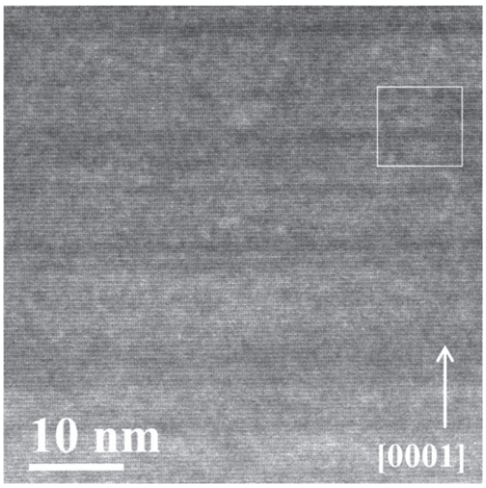

Figure 4. STEM-HAADF image depicting the irregular layering by Mn δ-doping; bright rectangle: region magnified in figure 5(a).

contrast variation between bright and dark lines as indicated by the dashed line. To shed more light onto the contrast variation, element specific EFTEM jump ratio imaging of the Mn L_{23} edge has been carried out, as displayed in figure 6(a).

Here the onset of the δ-doping (white dashed line) and the subsequent layering is clearly visible. The reason for the enhanced Mn signal at the onset of the δ-doped region (surface) is not yet completely clear but deemed to stem from segregation and/or initial nucleation of the doped layer.

From the extracted profile (figure 6(b)) of the Mn distribution image two aspects emerge: (i) approximately every 3 nm a layer has been introduced through the δ-process and its width is in the range 2–5 nm. (ii) Furthermore, when integrating perpendicular to the layers, an intensity ramp is detected. This is due to a thickness variation of the TEM foil, as determined by measuring the inelastic mean free path by means of EELS. The total relative thickness variation in the indicated area is going from 0.4 to 0.6.

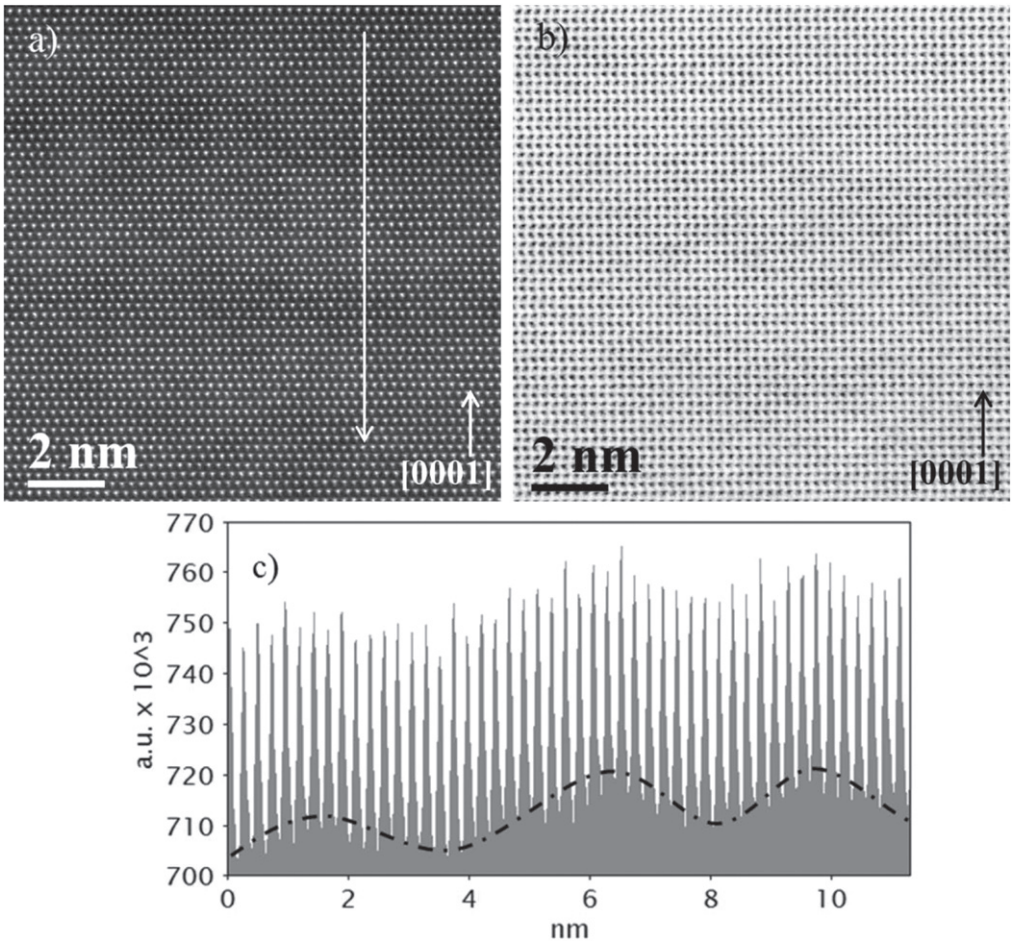

Figure 5. (a) High resolution HAADF image of Mn δ-doped GaN exhibiting contrast variation; white arrow: direction of profile extraction as depicted in (c); (b) corresponding ABF image providing information on the positions of Ga and N with a corresponding background variation as in (a); (c) extracted line-profile of (a) showing a sinusoidal contrast of the background of ~2% as indicated by the dashed line.

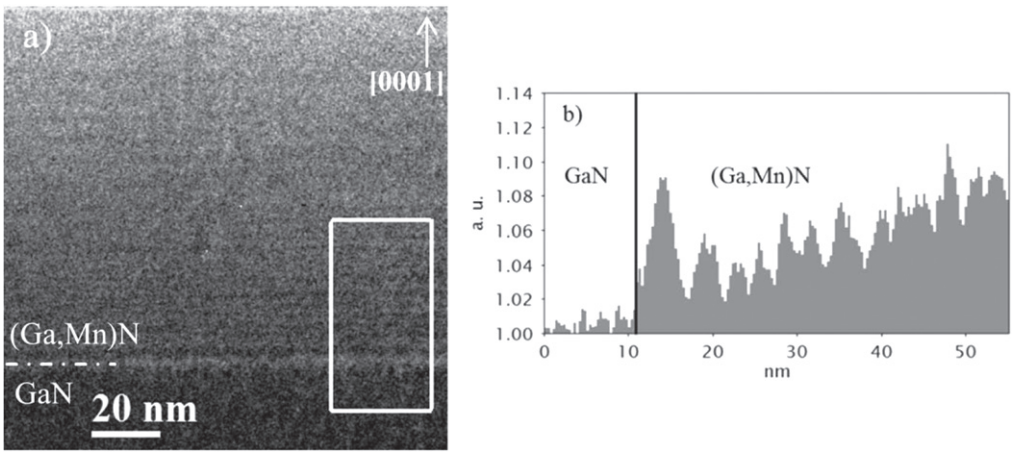

Figure 6. (a) EFTEM jump ratio map of the Mn L_{23} edge of Mn δ-doped GaN; white rectangle: region of profile extraction; (b) profile of the region marked in (a) showing a layering when moving from GaN into (Ga, Mn)N.

Spectroscopy has been carried out at several randomly chosen sample positions within the Mn-doped regions of GaN, and the EELS Ga L_{23}, N K, O K and Mn L_{23} edges have been quantified. Oxygen—detected in noticeable but similar amounts in all specimens—has been accounted for in the data analysis. To study the origin of the oxygen signal and particularly its impact on the quantification, a cross-section extracted from an analyzed specimen has also been fabricated using a focused ion beam (FIB) system. Combined STEM EELS and EDXS line-scans from the protective platinum towards GaN (shown in the STEM image of figure 7(a)) across the former (specimen)

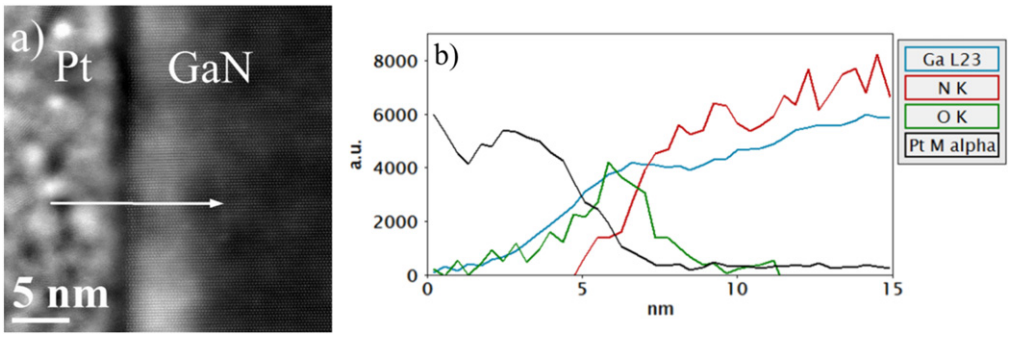

Figure 7. (a) HAADF image of the GaN-Pt interface with indication of the STEM-EELS-EDXS line-scan direction (white arrow); (b) extracted line-profiles for Ga, N, O and Pt confirming the presence of a 3 nm thick surface oxidation layer.

top-surface, have revealed an oxidized layer of 3 nm width.

In figure 7(b) a line-plot of the EELS Ga L_{23}, N K and O K edges and the EDXS Pt Mα signal, harnessing the relative merits of both techniques for the efficient detection of light and heavy elements is shown. For Pt (serving as a protection layer during FIB-cutting) and Ga, strong intermixing occurs, and is explained on one hand by surface roughness but also by Ga ion implantation into the Pt-protection layer (getting slightly oxidized as well). The quantitative compositional analysis of the homogenously Mn-doped region by EELS yields a rather uniform Mn concentration of 1.6 ± 0.1 at% averaged over several regions. The concentration values of the other elements are: Ga: 45.4 ± 0.6 at%; N: 48.8 ± 0.8 at% and O: 4.2 ± 1.1 at%, respectively.

For the analysis of the Mn delta-doped GaN, locations have been chosen such to assure that the beam has been placed either on or in between two bright lines. The average Mn concentration on bright layers is found to be 2.9 ± 0.5 at%, with Ga: 47.3 ± 1.4 at%; N: 46.8 ± 2.2 at% and O: 3.2 ± 3.2 at%. The average value of Mn in between the nominally doped layers is 1.3 ± 0.5 at% (with Ga: 47.6 ± 1.6 at%; N: 44.6 ± 2.4 at% and O: 6.5 ± 3.7 at%), being about 50% less compared to the doped layers but not vanishing. The high concentration variation of both layer-types reflects the heterogeneous deposition of Mn contrasting the homogenously doped sample. Due to this strong local inhomogeneity between the lines and within a line itself it is not feasible to give a meaningful average dopant concentration as for the homogenous sample.

3.2. Fe-doped GaN

The perspective functionalities of transition metal doped nitrides are expected to be realized not only with the dilute/homogeneous systems analyzed in the previous section, but also in phase separated materials such as e.g. (Ga, Fe)N. Particular growth conditions (as detailed in [6]) have led to a very narrow size-distribution of the nanostructures at a defined depth in the sample, as shown in figure 2(a), aggregating in a planar arrangement perpendicular to the growth direction. A comprehensive analysis of the structures and of their magnetic properties is reported in reference [23]. The HAADF imaging (figure 8(a)) reveals a typical 2-side facetted nanocrystal exhibiting a length of 25 nm and a height of approximately 17 nm. Figure 8(b) is a Fourier transform of figure 8(a) indicating an epitaxial relationship between the nanocrystal and the matrix. Higher resolution HAADF (figure 8(c)) and ABF (figure 8(d)) images do not show lattice distortions, supporting a coherent epitaxial growth mechanism.

To derive the composition of the nanocrystals, several of them (in samples with nominal doping concentrations of 0.25% and 0.5%) have been investigated and EELS as well as EDXS spectrum images have been recorded. Spectra collected from regions surrounding the nanocrystal (figure 9(b)) show no detectable presence of Fe confirming a confinement of the dopant within the nanocrystal. In a few non-typical cases, the nanocrystals display elemental inhomogeneity, as visible in figure 9. The Fe L_{23} map (figure 9(a)) and the respective spectra (figure 9(c)) indicate intensity differences within the nanocrystal, pointing to ~20% change in Fe concentration. This modulation is counterbalanced by an equal amount of Ga, where Fe is depleted (spectra not shown). Although these effects can be present, the overall variation in Fe content from crystal to crystal is by far larger.

Since absolute concentration measurements with each technique have shortcomings, we have performed data analysis in a relative manner with each technique comparing the two phases as shown in table 1. In this way systematic errors associated with low detection sensitivities and absorption for light elements in EDXS (N, O), and the uncertainties in the inner-shell ionization cross-sections for heavier elements (Ga, Fe) in the case for EELS can be avoided.

The general picture—averaging over all analyzed nanocrystals—is similar for the two techniques and shows similar trends. The Ga and N concentrations decrease to accommodate the large amounts of dopant and the extra oxygen. The Fe concentrations are on average about 2.5 times larger in the 0.5% Fe-doped sample than in the 0.25% Fe-doped one, yielding a ratio which is ~25% higher than the nominal one (with slight differences in Fe signal between the techniques). The situation on a per nanocrystal basis, showing the fluctuations in O and Fe content from nanocrystal to nanocrystal, is reported in figure 10. The dashed lines indicate the calculated average value for each technique within each graph. The

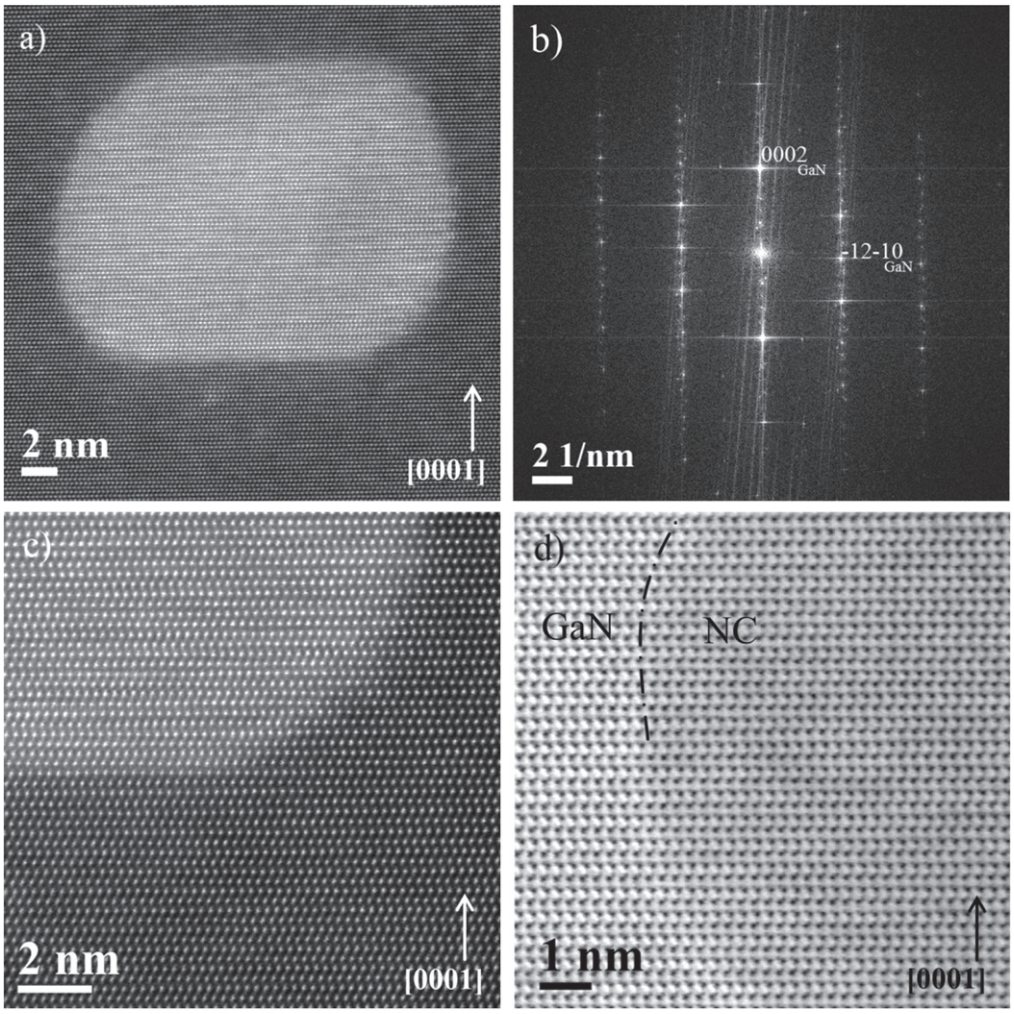

Figure 8. (a) High resolution STEM HAADF image of a typical nanocrystal; (b) Fourier transform, showing an aligned superposition of frequencies, fingerprint for an epitaxial relationship between nanocrystal and matrix; (c) coherent embedding of the nanocrystal in the matrix; (d) ABF image of a GaN/NC transition revealing no observable lattice distortion of the surrounding matrix.

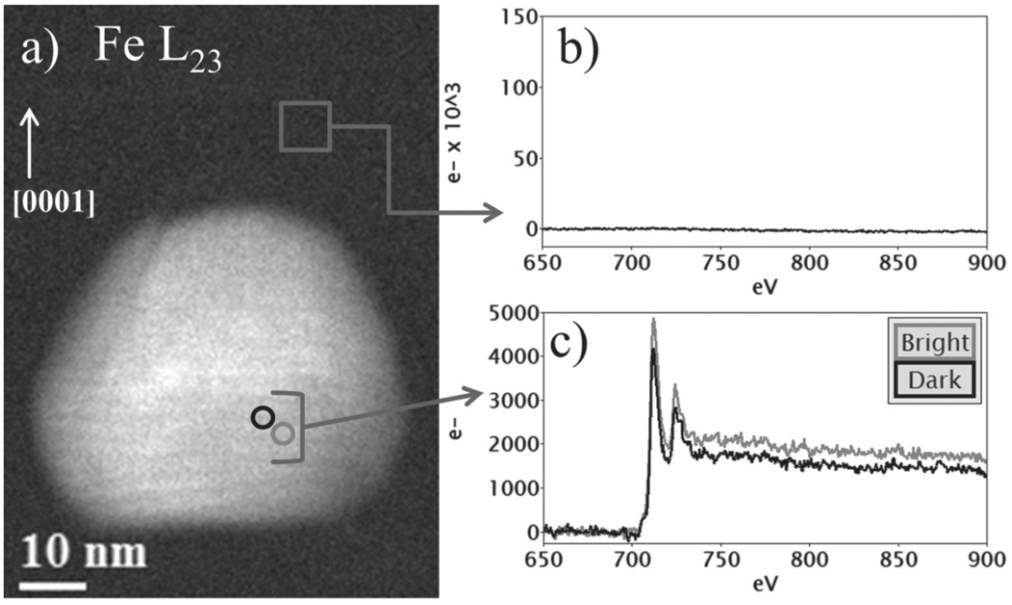

Figure 9. (a) Fe L_{23} EELS map from a nanocrystal; background-subtracted, integrated spectra from the spectrum image areas indicated in (a) for: (b) GaN matrix and (c) intensity differences within a Fe-rich nanocrystal.

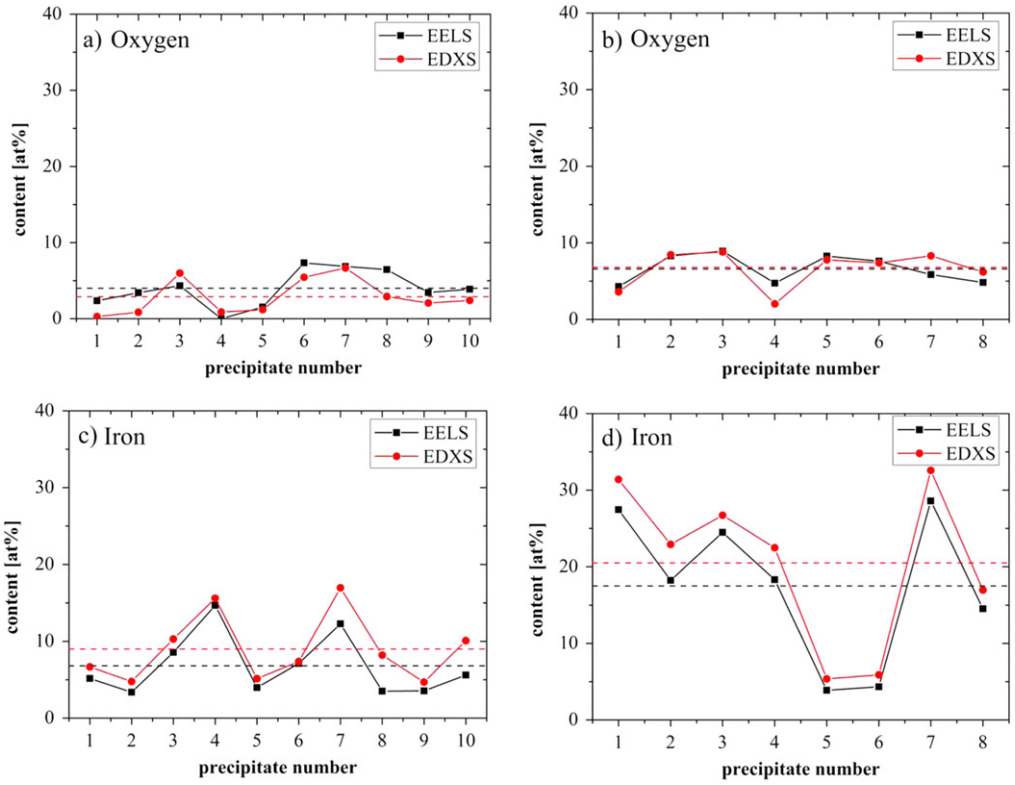

Figure 10. Variation of O and Fe content from nanocrystal to nanocrystal for: 0.25% Fe doping (a) and (c)) and 0.5% Fe doping (b) and (d)); dashed lines indicate the average value of Fe and O for each doping level.

Table 1. EELS and EDXS concentration ratio of Ga, N, Fe and O for two nominal doping concentrations (0.25% and 0.5%).

EELS	Ga	N	Fe	O
0.5%/0.25%	0.8 ± 0.1	0.9 ± 0.1	2.6 ± 1.9	1.7 ± 1.9
EDX	Ga	N	Fe	O
0.5%/0.25%	0.8 ± 0.1	0.9 ± 0.2	2.3 ± 1.5	2.3 ± 1.9

amount of oxygen in the 0.25% doped sample is as low as 0 at% and go up to 7 at%, whereas in the 0.5% specimen, the oxygen level reaches ∼9 at% and is never less than 2 at%.

On average, the O concentration is about twice as high in the 0.5% doped case as in the 25% one, including and assuming equal amounts of surface oxygen in both samples. The deviation between EELS and EDXS measurements is likely due to uncertainties in peak extraction at low energies for EDXS. The correlation between having more oxygen and increasing dopant concentrations falls short when looking at the individual nanocrystals, both in the 0.25% and in the 0.5% case Fe and O levels vary largely, indicating the formation of complex phases. In an attempt to separate out surface oxygen, in order to get an approximate value of the nanocrystal composition, a Ga_2O_3 layer has been assumed (being the only source of oxygen) and a stoichiometric fractional intensity of Ga (scaled to oxygen) has been subtracted from the nanocrystal. By back-adding different amounts of GaN matrix to the result and upon comparison with assumed γ'-$GaFe_3N$ and γ'-Fe_4N phases, no reasonable match has been achieved for a statistically significant number of nanocrystals hinting at a complex formation of mixed nitride oxides. To better account for the embedding of the nanocrystals in the matrix in a quantitative analysis, one has to make assumptions about the volumes of the crystal and correlate it with an absolute volumetric evaluation, e.g. by means of tomography. Alternatively, a particle extraction preparation process might be considered, taking into account that in this case of etching, consequent reduction of the nanocrystal size and modification of their stoichiometry can occur.

4. Conclusions

Modulated semiconductor structures require microscopic characterization techniques to unravel the distribution and chemistry of magnetic dopants, which critically determine the magnetic properties that are decisive for the performance of perspective devices such as spin filters (homogenous and 2D layers) or antiferromagnetic spintronic elements (nanocrystal based).

In this study, we have investigated structure and chemistry of different transition metal doped GaN systems, relevant for new technologies. Depending on the formation process, homogenous doping or layering in the case of Mn, and coherent formation of ordered Fe-rich nanocrystals in the case of Fe have been obtained. High-angle annular dark-field STEM as well as annular bright field in combination with analytical techniques such as EFTEM and quantitative EDXS

and EELS spectrum imaging have been chosen to investigate structure and homogeneity. Whereas the continuously doped samples show an even level of dopant material and negligible lattice modifications, the δ-doped material reveals a largely fluctuating amount of dopant, forming modulated, linear structures. Even in untreated regions, doping material is found to be significantly present. The introduction of a barrier layer is likely to foster the confinement of dopant to the desired regions.

In systems containing planar arrays of Fe-enriched coherently embedded nanocrystals, the modulation of growth parameters (substrate temperature and flow ratio) allows producing embedded nanocrystals with composition—and consequently magnetic response—on demand and studies in this direction are currently being undertaken. A success in this direction will give access to a system that can be tailored to be either ferromagnetic or antiferromagnetic at up to room temperature—depending on the phase of the nanocrystals—opening remarkable functionalities for both ferromagnetic and antiferromagnetic spintronics.

Acknowledgments

This work has been supported by the Austrian NANO Initiative within the project number: 819702, by the European Research Council (ERC Advanced Grant 227690) and by the Austrian Science Fundation (FWF Projects 22477, and 24471). The authors thank M Dienstleder, Graz Centre for Electron Microscopy, for technical support.

References

[1] Sato K *et al* 2010 First-principles theory of dilute magnetic semiconductors *Rev. Mod. Phys.* **82** 1633–90
[2] Bonanni A and Dietl T 2010 A story of high-temperature ferromagnetism in semiconductors *Chem. Soc. Rev.* **39** 528–39
[3] Jamet M *et al* 2006 High-Curie-temperature ferromagnetism in self-organized $Ge_{1-x}Mn_x$ nanocolumns *Nat. Mater.* **5** 653–9
[4] Yokoyama M, Yamaguchi H, Ogawa T and Tanaka M 2005 Zinc-blende-type MnAs nanoclusters embedded in GaAs *J. Appl. Phys.* **97** 10D3171
[5] Bonanni A *et al* 2011 Experimental probing of exchange interactions between localized spins in the dilute magnetic insulator (Ga, Mn)N *Phys. Rev.* B **84** 035206
[6] Bonanni A *et al* 2008 Controlled aggregation of magnetic ions in a semiconductor: an experimental demonstration *Phys. Rev. Lett.* **101** 135502
[7] Navarro-Quezada A *et al* 2010 Embedded magnetic phases in (Ga, Fe)N: key role of growth temperature *Phys. Rev.* B **81** 205206
[8] Devillers T *et al* 2012 Manipulating Mn-Mg_k cation complexes to control the charge- and spin-state of Mn in GaN *Sci. Rep.* **2** 7221–6
[9] Stefanowicz W *et al* 2010 Structural and paramagnetic properties of dilute $Ga_{1-x}Mn_xN$ *Phys. Rev.* B **81** 235210
[10] Bonanni A 2007 Ferromagnetic nitride-based semiconductors doped with transition metals *Semicond. Sci. Technol.* **22** R41–56
[11] Navarro-Quezada A, Devillers T, Li T and Bonanni A 2012 Planar arrays of magnetic nanocrystals embedded in GaN *Appl. Phys. Lett.* **101** 081911
[12] Brink H A, Barfels M M G, Burgner R P and Edwards B N 2003 A sub−50 meV spectrometer and energy filter for use in combination with 200 kV monochromated (S)TEMs *Ultramicroscopy* **96** 367–84
[13] Watanabe M, Horita Z and Nemoto M 1996 Absorption correction and thickness determination using the zeta factor in quantitative x-ray microanalysis *Ultramicroscopy* **65** 187–98
[14] Watanabe M and Williams D B 1999 Atomic-level detection by x-ray microanalysis in the analytical electron microscope *Ultramicroscopy* **78** 89–101
[15] Watanabe M and Williams D B 2006 The quantitative analysis of thin specimens: a review of progress from the Cliff-Lorimer to the new ζ-factor methods *J. Microsc.* **221** 89–109
[16] Gubbens A, Barfels M, Trevor C, Twesten R, Mooney P, Thomas P, Menon N, Kraus B, Mao C and McGinn B 2010 The GIF Quantum, a next generation post-column imaging energy filter *Ultramicroscopy* **110** 962–70
[17] Van Dyck D and Op de Beeck M 1996 A simple intuitive theory for electron diffraction *Ultramicroscopy* **64** 99–107
[18] Geuens P and Van Dyck D 2005 The s-state model for electron channeling in high-resolution electron microscopy *Adv. Imaging Electron Phys.* **136** 111–226
[19] Findlay S D, Shibata N, Sawada H, Okunishi E, Kondo Y, Yamamoto T and Ikuhara Y 2009 Robust atomic resolution imaging of light elements using scanning transmission electron microscopy *Appl. Phys. Lett.* **95** 191913
[20] Okunishi E, Ishikawa I, Sawada H, Hosokawa F, Hori M and Kondo Y 2009 Visualization of light elements at ultrahigh resolution by STEM annular bright field microscopy *Microsc. Microanal.* **15** 164–5
[21] Findlay S D, Shibata N, Sawada H, Okunishi E, Kondo Y and Ikuhara Y 2010 Dynamics of annular bright field imaging in scanning transmission electron microscopy *Ultramicroscopy* **110** 903–23
[22] Hytch M, Snoeck F and Kilaas R 1998 Quantitative measurement of displacement and strain fields from HREM micrographs *Ultramicroscopy* **74** 131–46
[23] Grois A, Devillers T, Li T and Bonanni A 2014 Planar array of self-assembled $Ga_xFe_{4-x}N$ nanocrystals in GaN: magnetic anisotropy determined via ferromagnetic resonance *Nanotechnology* **25** 395704